Bulgarian Chemical Communications, Volume 57, Issue 3 (pp. 282-294) 2025 *DOI: 10.34049/bcc.57.4.5705*

Eco-engineered ZnO nanoparticles *via Convolvulus prostratus* with Al- and Zr-doping: structural, mechanical, and antifungal enhancement for sustainable construction applications

N. J. Sai Varun[1], N. Sai Aishwarya Reddy[1], S. Pradeepa[1], H. S. Lalithamba[2]. Srilatha Rao[3], G. K. Prashanth[4,5*]

[1] *Department of Civil Engineering, Sir M. Visvesvaraya Institute of Technology, Bengaluru-562 157, India*
[2] *Department of Chemistry, Siddaganga Institute of Technology, Tumkur-572 103, India*
[3] *Department of Chemistry, Nitte Meenaskhi Institute of Technology, (Deemed to be University), Bengaluru-560 064, India*
[4] *Research and Development Centre, Department of Chemistry, Sir M. Visvesvaraya Institute of Technology, Bengaluru-562 157, India*
[5] *Visvesvaraya Technological University, Belagavi-590 018, India*

Received: June 07, 2025; Revised: July 05, 2025

This study presents the green synthesis of undoped and doped zinc oxide (ZnO) nanoparticles (NPs) using *Convolvulus prostratus* (*C. prostratus*) flower extract *via* the solution combustion synthesis (SCS) method. The plant extract, rich in phytochemicals, acts as a bio-reductant and combustion fuel, enabling eco-friendly nanoparticle fabrication. Aluminum (Al^{3+}) and zirconium (Zr^{4+}) ions were introduced as dopants at 3%, 5%, and 7% by co-dissolving their respective nitrates with zinc nitrate. Post-synthesis calcination at 600°C enhanced the crystallinity and phase purity of the resulting ZnO NPs. Structural characterization using powder X-ray diffraction (PXRD) confirmed a hexagonal wurtzite crystal structure with crystallite sizes ranging from 8.8 to 16.1 nm. Fourier transform infrared spectroscopy (FTIR), scanning electron microscopy with energy-dispersive X-ray spectroscopy (SEM-EDX), transmission electron microscopy (TEM), and ultraviolet-visible (UV-Vis) spectroscopy analyses revealed dopant-induced lattice distortion, morphological refinement, and tunable optical properties (band gap up to 3.77 eV). Mechanical testing of concrete blocks with the embedded ZnO NPs revealed that 7 mol% of Zr-doped ZnO imparted the highest compressive strength (49.96 MPa). Moreover, antifungal inspection demonstrated strong resistance against fungal colonization in doped samples. These results demonstrate the multifunctional potential of green-synthesized doped ZnO NPs in sustainable construction and antimicrobial material development.

Keywords: Green synthesis; zinc oxide NPs; *Convolvulus prostratus*; doping; aluminum; zirconium; PXRD; FTIR; SEM; sustainable concrete; antimicrobial activity; eco-friendly nanomaterials

INTRODUCTION

Nanotechnology has emerged as one of the most promising and transformative frontiers in material science, offering a vast spectrum of applications across disciplines such as medicine, catalysis, electronics, energy, and environmental protection [1-3]. Among various nanomaterials, zinc oxide NPs (ZnO NPs) have attracted significant attention due to their distinctive properties, including a wide band gap of 3.37 eV, high exciton binding energy (~60 meV), excellent chemical stability, biocompatibility, and multifunctional characteristics. These attributes render ZnO NPs suitable for diverse applications, ranging from ultraviolet (UV) shielding and gas sensing to photocatalysis, antimicrobial treatment, and optoelectronic device fabrication [4, 5].

Conventional synthesis techniques for ZnO NPs—such as sol-gel, hydrothermal, and chemical vapor deposition—are well-established but typically involve high energy consumption, toxic chemicals, and costly instrumentation. These drawbacks raise concerns about their long-term environmental sustainability and practical scalability [6–10]. In light of these limitations, green synthesis methodologies have gained considerable momentum as they align with the principles of green chemistry—minimizing hazardous by-products, reducing energy demands, and utilizing renewable natural sources.

Among green synthesis strategies, plant-mediated synthesis has emerged as a particularly eco-friendly and cost-effective approach. Plants are inherently rich in phytochemicals such as flavonoids, alkaloids, terpenoids, phenolics,

* To whom all correspondence should be sent:
E-mail: *prashanth_chem@sirmvit.edu*
prashaanthgk@gmail.com

glycosides, and proteins, which serve as natural reducing and stabilizing agents during nanoparticle formation. These bioactive compounds facilitate metal ion reduction and particle stabilization under mild, ambient conditions, enabling sustainable and large-scale nanoparticle synthesis without compromising efficiency or performance [11–16].

In our previous research, we have successfully synthesized ZnO NPs using a variety of plant-based materials, such as *Abutilon indicum*, *Melia azedarach*, *Indigofera tinctoria* [17], *Tamarindus indica*, *Punica granatum* [18], *Piper betle* [19], *Citrus limon* [20, 21], *Caesalpinia sappan* [22], *Mirabilis jalapa* [23], *Mimosa pudica* [24], *Simarouba glauca* [25] and explored their potential biological applications. In the present study, *Convolvulus prostratus*—commonly known as Shankhpushpi—was employed as a green precursor for the biosynthesis of ZnO NPs. A perennial herb from the *Convolvulaceae* family, *C. prostratus* is extensively distributed across India and has long-standing medicinal significance in Ayurvedic practices, where it is reputed for its neuroprotective, memory-enhancing, and cognitive-boosting properties. The flower extract of this plant is particularly rich in bioactive secondary metabolites such as flavonoids, phenolic acids, alkaloids, and coumarins, which are ideally suited for nanoparticle synthesis due to their reducing, chelating, and stabilizing capabilities [26–30].

Utilizing *C. prostratus* flower extract in nanoparticle synthesis presents dual benefits: (i) it leverages a renewable, non-toxic botanical source abundant in natural phytochemicals, and (ii) it enables the production of biocompatible, functionally enhanced ZnO NPs. To further modulate the physicochemical and functional properties of ZnO, doping with metal ions such as aluminum (Al^{3+}) and zirconium (Zr^{4+}) has been employed. Metal ion doping introduces structural and electronic modifications that can result in enhanced photoluminescence, modified band gap energy, and improved catalytic or antimicrobial performance, broadening the application potential of the resulting nanomaterials.

Concrete, one of the most widely used construction materials globally, is renowned for its mechanical strength, durability, and cost-effectiveness. However, modern sustainability challenges have necessitated innovation in concrete technology to develop more environmentally responsible and functionally superior materials. The integration of nanotechnology, particularly ZnO NPs—both undoped and doped—into concrete composites has shown promising results in this regard. ZnO NPs possess excellent photocatalytic, antimicrobial, and antifungal properties, which can significantly enhance the lifespan and hygienic quality of concrete structures [31–34]. Moreover, doping ZnO with Al and Zr further improves its surface reactivity and structural stability, optimizing its performance under real-world conditions.

From an ecological standpoint, the incorporation of ZnO NPs into concrete formulations can potentially reduce the overall carbon footprint by minimizing the dependence on traditional cement, a major contributor to CO_2 emissions. These nanomaterials also contribute to improved compressive strength, chemical resistance, and durability of concrete, while supporting circular construction practices through the efficient use of recycled aggregates and water. Additionally, the inherent antimicrobial and antifungal properties of doped ZnO help in mitigating microbial growth in moist environments, thereby preventing surface degradation and associated health hazards. The photocatalytic attributes further impart self-cleaning functionalities, making such materials especially suitable for use in public infrastructure and high-humidity settings [31–34]. Hence, the core objective of this research is to develop a green, simple, and sustainable route for synthesizing undoped and Al/Zr-doped ZnO NPs using *C. prostratus* flower extract through a solution combustion method. The synthesized nanomaterials were thoroughly characterized using modern analytical techniques such as X-ray diffraction (XRD), Fourier transform infrared spectroscopy (FTIR), scanning electron microscopy (SEM), and UV-Vis spectroscopy to understand their structural, morphological, and optical features. Furthermore, the synthesized NPs were embedded into concrete block formulations to evaluate their mechanical performance and antifungal activity. This work aims to contribute to the development of multifunctional, sustainable construction materials that combine environmental responsibility with superior structural and hygienic performance.

MATERIALS AND METHODS

Chemicals and reagents

Zinc nitrate hexahydrate [$Zn(NO_3)_2.6H_2O$, AR, [$ZrO(NO_3)_2.4H_2O$, AR, 99% SD fine], aluminum nitrate nonahydrate [$Al(NO_3)_3.9H_2O$, Fisher, AR, 99 %].

Flower collection

Fresh *C. prostratus* flowers (Figure 1) were collected from the vicinity of Malleswaram, Bengaluru, Karnataka, India. The collected flowers

were thoroughly cleaned with tap water to remove any adhering dust or soil, followed by rinsing with distilled water to eliminate residual impurities. The clean flowers were then shade-dried for 15 days to preserve the active phyto-constituents. After drying, the flowers were cut into small pieces and finely powdered using a mechanical grinder. The resulting powder was stored in an airtight container for further use in the green synthesis of NPs.

Figure 1. Flowers of *Convolvulus prostratus*

Preparation of flower extract

The aqueous extract of *C. prostratus* flowers was prepared using the Soxhlet extraction method. For this, 20.0 g of finely powdered, shade-dried *C. prostratus* flowers were loaded into the Soxhlet apparatus and extracted using 150 mL of double-distilled water as the solvent. The extraction process was carried out for several hours until the solvent in the siphon tube appeared clear, indicating complete extraction of water-soluble phytochemicals.

After completion of the extraction cycle, the resulting extract was allowed to cool to room temperature and then filtered using Whatman No. 1 filter paper to remove any residual plant debris. The clear aqueous filtrate was collected and stored in a clean, airtight container under refrigerated conditions for further use in the green synthesis of undoped and doped zinc oxide NPs.

Phytochemical analysis of C. prostratus flowers

To evaluate the presence of bioactive constituents responsible for the green synthesis of metal oxide NPs, a preliminary phytochemical screening of the aqueous extract of *C. prostratus* flowers was conducted using standard qualitative methods. The extract was tested for major phytochemical groups known to contribute to metal ion reduction, capping, and stabilization during nanoparticle formation.

The analysis confirmed the presence of various phytochemicals such as flavonoids, phenolic compounds, alkaloids, tannins, saponins, and glycosides, which are well known for their electron-donating ability and capability to form complexes with metal ions (Table 1). These compounds play a crucial role in converting metal precursors into stable NPs under ambient or combustion conditions.

The abundance of polyphenolic and flavonoid content in *C. prostratus* extract is particularly significant, as these compounds not only facilitate the reduction of metal ions (Zn^{2+}, Al^{3+}, Zr^{4+}) but also contribute to the stabilization of the resulting ZnO NPs by capping their surface, thereby preventing agglomeration.

Table 1. Phytochemical constituents present in *C. prostratus* flower extract

S. No.	Phytochemical group	Observation	Results (+/-)
1	Alkaloids	White precipitate (Wagner's test)	+
2	Flavonoids	Yellow coloration (Alkaline reagent test)	+
3	Phenolic compounds	Blue-black color (Ferric chloride test)	+
4	Tannins	Greenish-black color (Lead acetate test)	+
5	Saponins	Stable froth formation (Foam test)	+
6	Glycosides	Brick-red precipitate (Keller–Killiani test)	+
7	Terpenoids	Reddish-brown interface (Salkowski's test)	+/−
8	Proteins	Violet color (Biuret test)	−

Note: (+) Present; (−) Absent; (+/−) Trace or weak presence

Synthesis of undoped, Al- and Zr-doped ZnO NPs by solution combustion method

The solution combustion synthesis (SCS) method was employed for the green synthesis of undoped and doped zinc oxide NPs using *C. prostratus* flower extract as a natural bio-reductant and fuel. The procedure followed a modified version of the methodology reported in our previous publication.

For the synthesis of undoped ZnO NPs, 2.0 g of zinc nitrate hexahydrate was dissolved in 20 mL of double-distilled water under constant magnetic stirring until a clear solution was obtained. To this solution, 5.0 mL of the prepared plant extract was added and thoroughly mixed. The homogeneous mixture was then transferred into a ceramic crystallizing dish and introduced into a preheated muffle furnace set at 400 ± 15°C. Within a few minutes, the solution formed a transparent gel which subsequently underwent spontaneous combustion due to the presence of the bio-fuel, resulting in a voluminous, fluffy powder of ZnO NPs.

For the synthesis of doped ZnO NPs, the same procedure was followed with the addition of dopant precursors—aluminum nitrate nonahydrate or zirconyl nitrate tetrahydrate (at specific molar

substitution levels of x = 0.03, 0.05, and 0.07), following the general formula $Zn_{1-x}M_xO$, where M = Al or Zr. The calculated amount of dopant salt was co-dissolved with zinc nitrate in the aqueous medium before the addition of the plant extract, ensuring uniform distribution of dopant ions within the precursor solution.

Physico-chemical characterization of NPs

Various analytical methods were employed to characterize the synthesized NPs, including PXRD, FTIR spectroscopy, SEM with EDAX, TEM, and UV-Vis spectroscopy. XRD patterns were recorded using a Shimadzu PXRD 7000 diffractometer with Cu Kα radiation (λ = 1.5406 Å) over a 2θ range of 30˚–75˚. The surface morphology was analyzed with a JEOL JSM 6390 scanning electron microscope. UV-Vis absorption spectra were obtained using a Perkin Elmer Lambda 35 spectrophotometer in diffuse reflectance mode, covering wavelengths between 200 and 800 nm. FTIR spectroscopy was used to study chemical bonding in the ZnO NPs, employing a Bruker Alpha-1 spectrometer with KBr windows and a resolution of 2 cm^{-1} over the range of 400–4000 cm^{-1}. TEM measurement was carried out on a Philips 200 instrument.

- *Concrete block preparation and mechanical testing conditions*. Concrete blocks were prepared with a cement: sand: aggregate mix ratio of 1:2:4, using a water-to-cement ratio of 0.5. The blocks were cured for 28 days in water at 27 ± 2°C before testing. All compressive strength measurements were carried out following IS 516–1959 in triplicate, and the average values are reported.
- *Mechanical strength testing*. After curing, compressive strength tests were carried out according to IS 516–1959 using a compression testing machine. Each value reported is an average of three replicate measurements.
- *Antifungal activity testing*. The antifungal testing involved block exposure to fungal cultures with observations made after 72 h. Although inhibition zones were noted visually, no numerical data such as inhibition diameters or CFU counts were recorded in this study. This is now acknowledged as a limitation, and future work will incorporate quantitative microbiological analysis. The antifungal activity was tested in triplicate to ensure reproducibility.

RESULTS AND DISCUSSION

Formation mechanism of undoped and doped ZnO NPs

The green synthesis of undoped and doped ZnO NPs using *C. prostratus* flower extract operates through a phytochemical-mediated solution combustion mechanism. The extract, rich in bioactive compounds such as flavonoids, phenolics, alkaloids, tannins, and saponins, plays a critical role in the reduction of metal precursors, stabilization of nanoparticle surfaces, and control over particle growth and morphology. These naturally occurring phytochemicals not only serve as eco-friendly reducing and stabilizing agents but also act as combustion fuels during synthesis. In the initial stage, $Zn(NO_3)_2{\cdot}6H_2O$ and the plant extract are mixed in aqueous medium, where phytochemicals chelate with Zn^{2+} ions through functional groups such as hydroxyl, carbonyl, or amine. This interaction results in the formation of a Zn^{2+}–phytocomplex, which is further transformed into a gel-like precursor under heating. The addition of dopant salts such as aluminum nitrate or zirconyl nitrate enables the co-complexation of Al^{3+} or Zr^{4+} ions into the gel matrix, forming $Zn_{1-x}M_xO$ (M = Al or Zr; x = 0.03, 0.05, 0.07) compositions. Upon heating the precursor gel in a preheated muffle furnace at around 400 ± 15°C, spontaneous combustion takes place due to the redox reaction between the oxidizing metal nitrates and the reducing organic compounds in the extract. This exothermic reaction results in the rapid evolution of gases such as CO_2, NO_x, and H_2O vapor, which causes the gel to swell and combust, yielding voluminous, porous, and fine ZnO NPs. The presence of phytochemicals ensures uniform combustion and prevents the agglomeration of NPs by acting as surface capping agents. In the case of doped ZnO, the Al^{3+} or Zr^{4+} ions substitute Zn^{2+} ions within the crystal lattice of ZnO during the combustion process. These dopant ions cause local distortions in the crystal lattice, affect the crystallite size, and modify the electronic structure, resulting in enhanced optical and structural properties of the final NPs. The uniform distribution of dopants is facilitated by the homogenous mixing in the aqueous phase prior to combustion. To improve crystallinity and remove residual organic content, all synthesized nanoparticle samples are further subjected to calcination at 600°C for 1 h. This step also promotes better dopant incorporation into the ZnO matrix and ensures the development of a pure wurtzite crystalline structure.

The green solution combustion synthesis using *C. prostratus* flower extract provides a simple, efficient, and eco-friendly route to fabricate undoped and Al/Zr-doped ZnO NPs. The mechanism involves complexation, gel formation, combustion-driven nanoparticle generation, and thermal treatment—all aided by the multifunctional properties of the phytochemicals present in the flower extract. A

proposed mechanism for the formation of ZnO NPs is illustrated in Figure 2.

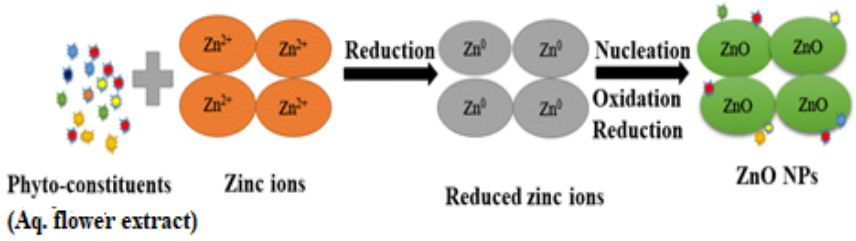

Figure 2. Plausible mechanism of formation of ZnO-NPs

Powder X-ray diffraction (PXRD) analysis

The crystalline nature and phase purity of the synthesized undoped and doped ZnO NPs were confirmed through X-ray diffraction (XRD) analysis. The diffraction patterns of all samples, as shown in Figure 3, exhibit sharp and intense peaks, indicating high crystallinity. The observed diffraction peaks at 2θ values of approximately 31.8° (100), 34.4° (002), 36.2° (101), 47.5° (102), 56.6° (110), 62.9° (103), and 68.0° (112) correspond to the hexagonal wurtzite structure of ZnO with the space group *P6₃mc*. These peak positions are in good agreement with the standard JCPDS card no. 36-1451, confirming the successful formation of ZnO NPs.

Importantly, no additional peaks corresponding to impurity phases such as Al_2O_3 or ZrO_2 were detected in the doped samples, indicating the successful substitution of Al^{3+} and Zr^{4+} into the Zn^{2+} lattice without altering the host ZnO phase. This implies that doping did not disturb the hexagonal crystal structure and that the synthesized NPs maintained high phase purity. The consistency in peak positions across all samples further supports this conclusion.

The average crystallite size (D) of the NPs was estimated using the Debye–Scherrer equation, $D = (k\lambda)/(\beta\cos\theta)$, where k=0.9, λ=0.15406 nm (Cu Kα radiation), β is the full width at half maximum (FWHM) of the most intense peak (101 plane), and θ is the corresponding Bragg angle. Crystallite sizes ranged from 8.8 nm to 16.1 nm, depending on the dopant type and concentration. The largest crystallite size (16.1 nm) was observed for $Zn_{0.93}Zr_{0.07}O$, while the smallest size (8.8 nm) was found in $Zn_{0.93}Al_{0.07}O$, indicating that Al doping at higher concentration inhibited crystal growth more significantly than Zr doping.

Additionally, the micro-strain (ε) in the samples was calculated using the relation $\varepsilon = (\beta\cos\theta)/4$. The strain values varied from 0.136 ($Zn_{0.93}Zr_{0.07}O$) to 0.222 ($Zn_{0.95}Zr_{0.05}O$), showing that doping induces lattice distortion, which is slightly more pronounced in Zr-doped samples due to the larger ionic radius of Zr^{4+} compared to Zn^{2+}.

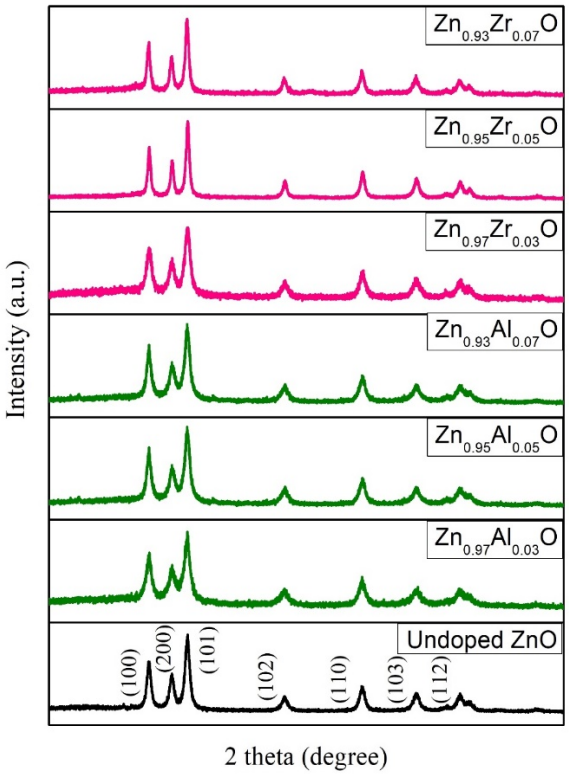

Figure 3. PXRD patterns of undoped and doped ZnO NPs

The detailed XRD parameters, including peak position (2θ), FWHM, intensity, crystallite size (D), and micro-strain (ε) for all samples, are summarized in Table 2.

Table 2. 2θ, FWHM, intensity (101) plane, D, and micro-strain (ε) of NPs

Sample	Peak position (2θ)	FWHM (2θ)	Intensity (cps)	D (nm) crystallite size	ε
Undoped ZnO	36.15	0.67	762.3	12.5	0.1763
$Zn_{0.97}Al_{0.03}O$	36.16	0.81	416.47	10.3	0.213
$Zn_{0.95}Al_{0.05}O$	36.11	0.69	572	12.1	0.1815
$Zn_{0.93}Al_{0.07}O$	36.11	0.74	570	8.8	0.194
$Zn_{0.97}Zr_{0.03}O$	36.11	0.72	572.5	11.6	0.189
$Zn_{0.95}Zr_{0.05}O$	36.15	0.86	372	9.7	0.222
$Zn_{0.93}Zr_{0.07}O$	36.11	0.52	585.2	16.1	0.136

Table 3. FTIR spectral band assignments of pure and doped ZnO NPs

Observed wavenumber (cm^{-1})	Assignment	Sample(s)	Reference
443.92	Zn–O stretching vibration (wurtzite phase)	ZnO	[35, 36]
439.7–448.71	Shifted Zn–O stretching due to Al^{3+} doping	$Zn_{0.97}Al_{0.03}O$ to $Zn_{0.93}Al_{0.07}O$	[37, 38]
445.61–479.90	Shifted Zn–O stretching due to Zr^{4+} doping	$Zn_{0.97}Zr_{0.03}O$ to $Zn_{0.93}Zr_{0.07}O$	[39, 40]
3424.79–3442.51	O–H stretching of surface hydroxyl or adsorbed water	All samples	[37, 38]
1384.27–1403.34	Symmetric stretching of CO_3^{2-} or C=O group (adsorbed CO_2)	Al- and Zr-doped ZnO	[39, 41]
1116.33–1117.68	C–O stretching (possibly from residual organic precursors)	Al- and Zr-doped ZnO	[39, 41]

FTIR analysis

The Fourier transform infrared (FTIR) spectra of pure and doped ZnO NPs synthesized by the solution combustion method are presented in Figure 4 and Table 3. The FTIR data provide crucial insights into the bonding environment, functional groups, and lattice distortions arising from Al^{3+} and Zr^{4+} doping.

In the undoped ZnO sample, a prominent absorption band appears at 443.92 cm^{-1}, corresponding to the Zn–O stretching vibration, confirming the formation of the wurtzite phase of ZnO [35, 36]. A broad band around 3424.79 cm^{-1} is assigned to the O–H stretching vibration arising from surface-adsorbed moisture or hydroxyl groups [37].

Doping with Al^{3+} leads to noticeable shifts in the Zn–O vibration bands to 439.76 cm^{-1} ($Zn_{0.97}Al_{0.03}O$), 448.71 cm^{-1} ($Zn_{0.95}Al_{0.05}O$), and 443.65 cm^{-1} ($Zn_{0.93}Al_{0.07}O$). These variations reflect substitutional incorporation of Al^{3+} into the ZnO lattice, resulting in minor distortions due to the smaller ionic radius of Al^{3+} (0.53 Å) compared to Zn^{2+} (0.74 Å) [38]. Additionally, distinct bands at ~ 1116–1117 cm^{-1} and ~ 1384–1403 cm^{-1} are observed in the doped samples, which are attributed to C–O stretching vibrations and symmetric stretching of carbonate groups, respectively. These likely originate from residual organic precursors or atmospheric CO_2 adsorption during synthesis and handling [39].

Similarly, Zr-doped ZnO samples show Zn–O stretching peaks at 445.61 cm^{-1} ($Zn_{0.97}Zr_{0.03}O$), and further shifting to higher wavenumbers in $Zn_{0.95}Zr_{0.05}O$ (479.90 cm^{-1}) and $Zn_{0.93}Zr_{0.07}O$ (479.29 cm^{-1}), indicating substantial lattice distortion due to the substitution of larger Zr^{4+} ions (0.72 Å) [40]. Broad absorption in the region of 3418–3442 cm^{-1} in these samples confirms the presence of surface hydroxyl groups. The presence of bands around 1116 cm^{-1} and 1403 cm^{-1} in Zr-doped samples is consistent with the features seen in Al-doped ZnO. These spectral shifts and the appearance of new bands suggest successful incorporation of dopant ions into the ZnO matrix and modification of surface chemistry, which are expected to impact the material's physicochemical and optical properties.

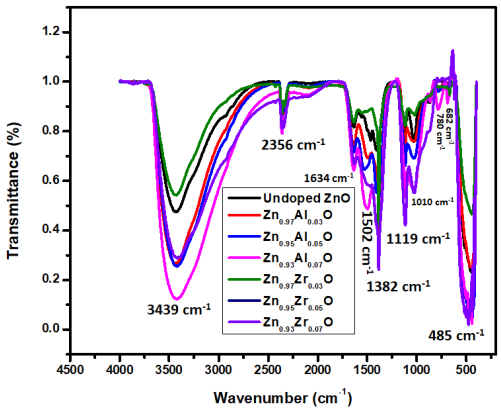

Figure 4. FTIR spectra of (black) undoped ZnO, (red) 3 mol % Al-doped ZnO, (blue) 5 mol %Al-doped ZnO, (pink) 7 mol % Al-doped ZnO, (green) 3 mol % Zr-doped ZnO, (navy blue) 5 mol % Zr-doped ZnO, and (purple) 7 mol % Zr-doped ZnO.

SEM and EDX analysis of NPs

- *Undoped ZnO NPs*. The SEM image of undoped ZnO NPs (Figure 5a) shows highly agglomerated structures with irregular morphology. The particles appear to be interconnected, forming porous clusters that are likely a result of rapid combustion reactions during synthesis, which release large volumes of gases (CO_2, H_2O) that create voids in the matrix. This sponge-like morphology is typical of combustion-synthesized ZnO nanostructures [42]. The corresponding EDX spectrum (Figure 5b) confirms the presence of elemental Zn and O, with no detectable impurities, validating the purity of the synthesized ZnO. The atomic percentages of Zn and O are 73.95% and 26.05%, respectively, consistent with stoichiometric ZnO.
- *7 mol% Al-doped ZnO NPs*. Upon doping with 7 mol% aluminum, the SEM micrograph (Figure 5c) shows a noticeable morphological transformation. The particles become finer and exhibit a more uniform distribution compared to undoped ZnO, suggesting that Al^{3+} ions help regulate the nucleation and growth processes during synthesis. The decrease in agglomeration and increased surface roughness can enhance the surface area and catalytic properties of the material [43]. EDX analysis (Figure 5d) confirms the successful incorporation of aluminum, with elemental signals for Zn, O, and Al clearly observed. The calculated Al content aligns well with the intended doping level, with a measured atomic percentage of 2.91%.
- *7 mol% Zr-doped ZnO NPs*. The SEM image of Zr-doped ZnO (Figure 5e) reveals a denser, more compact morphology with larger clusters than both undoped and Al-doped samples. The Zr doping appears to promote grain growth and aggregation due to the ionic size mismatch between Zr^{4+} and Zn^{2+}, which induces lattice strain and modifies crystallization behavior [44]. This results in a tightly packed structure with reduced porosity. The EDX spectrum (Figure 5f) confirms the presence of Zr along with Zn and O, validating successful doping. The atomic percentage of Zr is 3.11%, closely matching the theoretical 7 mol% substitution. The TEM image of undoped ZnO NPs (Figure 5g) reveals quasi-spherical particles with a moderate degree of agglomeration, consistent with observations from SEM analysis. Individual particles are generally in the nanoscale range, with estimated sizes between 20–40 nm, and appear to be embedded within loosely packed clusters. The relatively uniform contrast across the particles suggests good crystallinity, while the slight aggregation may stem from van der Waals interactions and the absence of surface stabilizers. The particle boundaries are discernible, indicating a distinct nanocrystalline nature. These features further confirm that the combustion synthesis route effectively yields nanosized ZnO with fine morphological control.

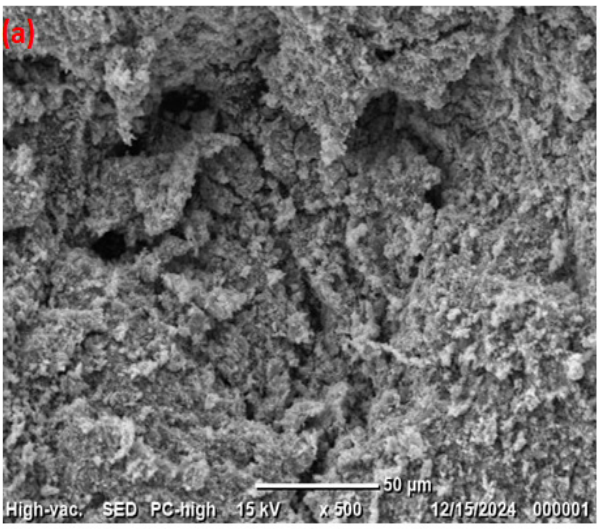

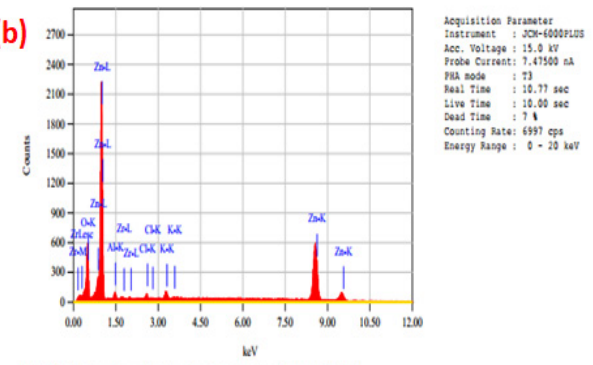

Thin Film Standardless Standardless Quantitative Analysis(Oxide)
Fitting Coefficient : 0.7195
Total Oxide : 24.0

Element	(keV)	Mass%	Counts	Sigma	Mol%	Compound	Mass%	Cation	K
O *		19.92					ND		
Al K*	1.486	0.87	326.86	0.17	1.30	Al2O3	1.64	0.62	0.1145
Cl K*	2.621	0.70	188.10	0.10	1.60	Cl	0.70	0.00	0.1598
K K*	3.312	1.40	326.37	0.17	1.46	K2O	1.69	0.69	0.1853
Zn K* (Ref.)	8.630	77.11	3324.78	2.49	95.64	ZnO	95.97	22.72	1.0000
Zr L*		ND					ND		
Total		100.00			100.00		100.00	24.04	

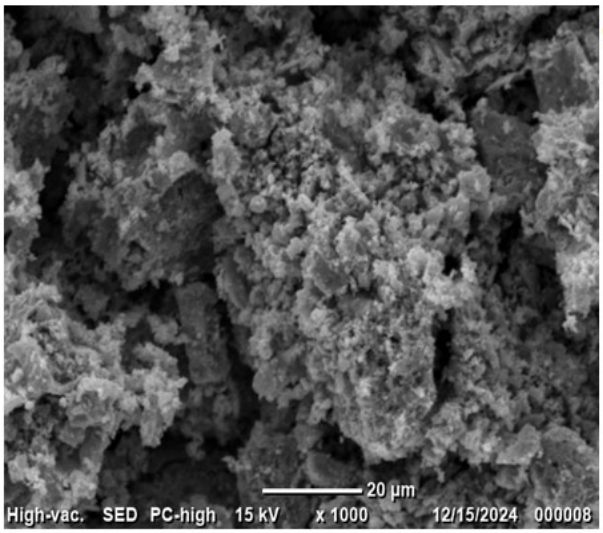

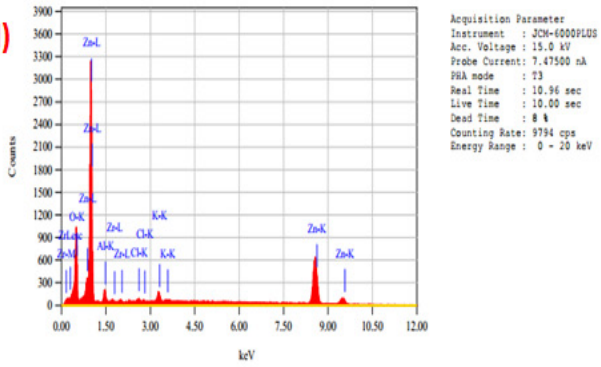

Thin Film Standardless Standardless Quantitative Analysis(Oxide)
Fitting Coefficient : 0.7085
Total Oxide : 24.0

Element	(keV)	Mass%	Counts	Sigma	Mol%	Compound	Mass%	Cation	K
O		20.23					ND		
Al K	1.486	1.54	640.99	0.21	2.32	Al2O3	2.90	1.08	0.1145
Cl K	2.621	0.68	204.44	0.10	1.57	Cl	0.68	0.00	0.1598
K K	3.312	2.68	691.83	0.21	2.80	K2O	3.23	1.30	0.1853
Zn K* (Ref.)	8.630	74.87	3577.48	2.34	93.31	ZnO	93.18	21.73	1.0000
Zr L*		ND					ND		
Total		100.00			100.00		100.00	24.11	

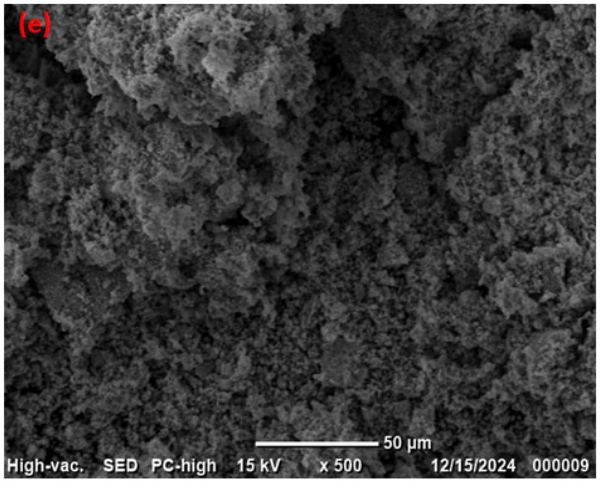

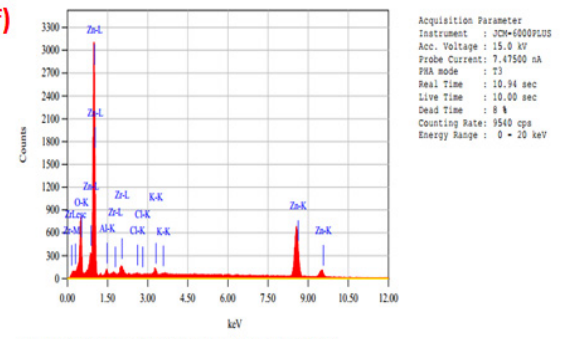

Thin Film Standardless Standardless Quantitative Analysis(Oxide)
Fitting Coefficient : 0.7202
Total Oxide : 24.0

Element	(keV)	Mass%	Counts	Sigma	Mol%	Compound	Mass%	Cation	K
O		20.37					ND		
Al K	1.486	0.75	319.28	0.16	1.16	Al2O3	1.41	0.52	0.1145
Cl K	2.621	0.37	112.01	0.08	0.86	Cl	0.37	0.00	0.1598
K K	3.312	1.62	425.74	0.18	1.73	K2O	1.95	0.78	0.1853
Zn K (Ref.)	8.630	71.54	3491.19	2.30	91.35	ZnO	89.04	20.61	1.0000
Zr L	2.042	5.36	521.74	0.59	4.90	ZrO2	7.23	1.11	0.5010
Total		100.00			100.00		100.00	23.02	

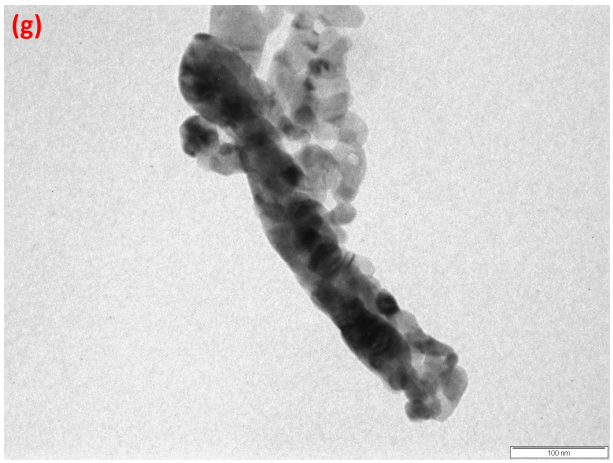

Figure 5 (a) SEM and (b) EDX of undoped ZnO NPs; (c) SEM and (d) EDX of 7 mol % Al-doped ZnO NPs; (e) SEM and (f) EDX of 7 mol % Zr-doped ZnO NPs (g) TEM image of undoped ZnO NPs

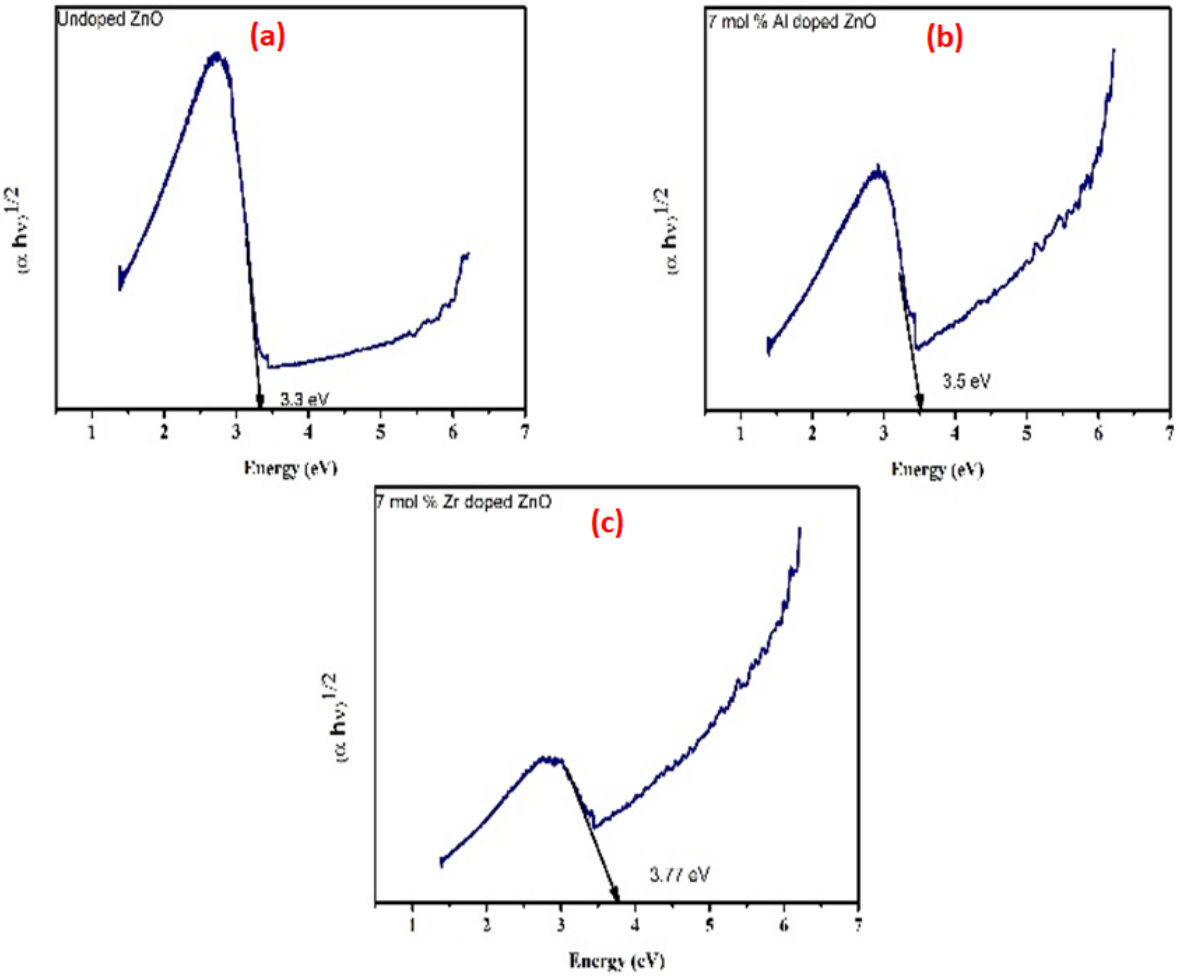

Figure 6. Band gap calculation of (a) undoped ZnO NPs, (b) 7 mol % Al-doped ZnO NPs, and (c) 7 mol % Zr-doped ZnO NPs

Mechanical properties of concrete blocks

The results of the experimental study are visually represented in the comparative bar graph, highlighting both the cubic weight (kg) and compressive strength (MPa) of four different types of concrete blocks—Plain concrete block, ZnO mixed block, Al + ZnO mixed block, and Zr + ZnO mixed block (Table 4 and Figure 7). The evaluation of these samples allows for an understanding of how nanomaterial admixtures, particularly doped ZnO variants, affect the physical and mechanical properties of concrete.

In terms of cubic weight, all concrete blocks show very close values, ranging from 8.25 kg to 8.32 kg. The plain concrete block recorded a weight of 8.25 kg, while the ZnO, Al + ZnO, and Zr + ZnO mixed blocks had weights of 8.3 kg, 8.32 kg, and 8.31 kg, respectively. These marginal differences indicate that the incorporation of ZnO and its doped variants in small percentages (0.5%–1%) does not significantly influence the overall density of the concrete. This consistency confirms that mix proportions and compaction practices were uniformly maintained across all samples, allowing a fair comparison of their mechanical performance.

When examining compressive strength, distinct variations become evident. The plain concrete block achieved a compressive strength of 35 MPa, serving as the baseline for performance comparison. Interestingly, the inclusion of undoped ZnO led to a reduction in strength to 32 MPa, suggesting that ZnO alone may slightly disrupt the internal bonding or hydration processes. A further drop was observed with Al + ZnO mixed blocks, which registered a compressive strength of 30.5 MPa. This could be attributed to agglomeration of NPs or interference with cement hydration at higher dosages, highlighting the importance of optimizing the amount and dispersion of such additives.

In contrast, the Zr + ZnO mixed block demonstrated superior performance, achieving a compressive strength of 37.5 MPa, the highest among all tested samples. This suggests that Zr doping significantly enhances the pozzolanic or micro-filling effects of ZnO NPs, potentially improving the microstructure of the cement matrix and resulting in higher load-bearing capacity. The effectiveness of Zr as a dopant may stem from its ability to promote better hydration reactions or denser matrix formation compared to Al.

The results clearly indicate that while nano-admixtures can modify concrete properties, their effectiveness strongly depends on the type and concentration of the dopant. Zr-doped ZnO, in particular, stands out as a promising additive for enhancing compressive strength without compromising the workability or mass of the concrete. However, the decrease in strength observed with ZnO and Al-doped mixes also underscores the need for further microstructural studies to understand their dispersion behavior and interaction with the cement matrix.

Table 4. Compressive strength test values

S. No	DOC	Cubic weight (Kg)	Load (KN)	Strength (M Pa)	Admixture
1	25/11	8.520	744.1	33.07	-
2	25/11	8.010	908.7	40.39	-
3	25/11	8.370	705.4	31.35	ZnO (0.5%)
4	25/11	8.270	754.6	33.35	ZnO (1%)
5	25/11	8.300	695.9	30.92	Al-doped ZnO – 3 mol % (0.5%)
6	25/11	8.720	466.1	20.71	Al-doped ZnO – 3 mol % (1%)
7	25/11	8.850	1124.1	49.96	Al-doped ZnO – 5 mol % (0.5%)
8	25/11	8.190	534.4	23.75	Al-doped ZnO – 5 mol % (1%)
9	25/11	8.130	552.6	24.56	Al-doped ZnO – 7 mol % (0.5%)
10	25/11	8.290	703.7	31.27	Al-doped ZnO – 7 mol % (1%)
11	25/11	8.300	983.8	43.72	Zr-doped ZnO – 3 mol % (0.5%)
12	25/11	8.320	753.8	33.50	Zr-doped ZnO – 3 mol % (1%)
13	25/11	8.380	869.8	38.65	Zr-doped ZnO – 5 mol % (0.5%)
14	25/11	8,290	799.9	35.55	Zr-doped ZnO – 5 mol % (1%)
15	25/11	8.530	680.9	30.26	Zr-doped ZnO – 7 mol % (0.5%)
16	25/11	8.110	825.9	36.79	Zr-doped ZnO – 7 mol % (1%)

Figure 7. Compressive strength

- *Antifungal activity evaluation through visual inspection*. The antifungal efficacy of the developed concrete blocks was assessed through a simple yet effective visual inspection method. As depicted in the image, two types of concrete blocks were compared: an antifungal block embedded with ZnO NPs (doped and/or undoped) and a plain concrete block without any nanoparticle incorporation. After exposure to conditions favorable for microbial growth, particularly high humidity, the blocks were examined for signs of fungal colonization on their surfaces. The results are presented in Figure 8.

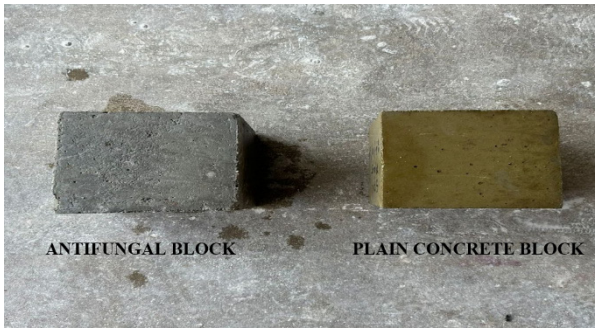

Figure 8. Comparison of antifungal block and plain concrete block

The plain concrete block displayed a visibly discolored surface with potential spots that are typically associated with initial stages of fungal growth. In contrast, the antifungal block exhibited a cleaner, uniformly gray surface, with no visible signs of fungal growth, indicating its superior resistance to microbial contamination. This clear visual distinction confirms the antifungal activity of the ZnO nanoparticle-enhanced concrete. The NPs likely disrupt fungal cell membranes through the generation of reactive oxygen species (ROS), a mechanism further enhanced by doping with Al and Zr, which increases surface reactivity. Such antifungal performance not only prolongs the lifespan of the concrete but also ensures improved sanitation, particularly in moisture-prone environments such as bathrooms, basements, public facilities, and humid climates.

The antifungal efficacy of ZnO NPs incorporated in concrete might largely be attributable to their surface exposure, facilitating direct interaction with fungal cells. ZnO is recognized for producing reactive oxygen species (ROS) that compromise fungal cell membranes [45]. The antifungal action is thought to be surface-mediated, resulting from NPs included inside the concrete rather than applied as a coating, and is derived from those at the exposed concrete interface [46]. This indicates that fungal proliferation is predominantly suppressed at the block surface where the ZnO NPs are available. The statement means that the presence of ZnO NPs effectively inhibits fungal growth, particularly at the surface where the NPs are located. This localized effect suggests that the ZnO NPs are interacting with and suppressing fungal proliferation directly at the site of their application [47]. This study did not implement a distinct surface coating approach; the NPs were uniformly integrated during the concrete mixing process.

The antifungal activity of ZnO NPs embedded in concrete is likely due to their surface-exposed presence, enabling direct interaction with fungal cells. Since the NPs were uniformly dispersed during concrete mixing and not applied as a surface coating, the inhibition is primarily surface-mediated**,** resulting from exposed NPs at the block surface.

A schematic diagram (Figure 9) illustrates the proposed cellular-level antifungal mechanisms by which ZnO NPs may inhibit fungal growth. These mechanisms include: (A) generation of ROS inducing lipid peroxidation, (B) disruption of fungal membranes, (C) pore formation, (D) leakage of intracellular content, (E) metal ion release, (F) DNA intercalation and fragmentation, (G) gene expression alterations, (H) amplified oxidative stress, (I) mitochondrial cytochrome C release triggering apoptosis, (J) ribosomal disassembly, and (K) inhibition of biofilm formation *via* binding to extracellular polymeric substances (EPS).

Although these mechanisms have been widely reported for nanoparticle–fungus systems, further research is required to confirm and visualize such effects specifically within concrete matrices.

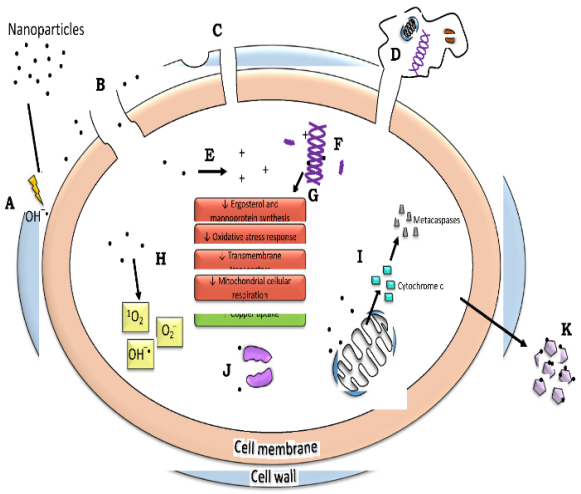

Figure 9. The cellular-level antifungal mechanisms of NPs involve multiple pathways: (A) induction of ROS that trigger lipid peroxidation; (B) interaction with and disruption of the fungal cell wall and membrane through adsorption and embedment; (C) formation of pits and pores; (D) leakage of intracellular contents including DNA and organelles; (E) release of metal ions; (F) intercalation with DNA leading to its condensation and fragmentation; (G) alterations in gene expression; (H) enhanced ROS production; (I) mitochondrial release of cytochrome C into the cytoplasm, which elevates metacaspase activity and initiates apoptotic pathways; (J) disassembly of ribosomes; and (K) binding to extracellular polymeric substances (EPS), thereby inhibiting biofilm development [47].

CONCLUSION

The green synthesis of undoped and Al/Zr-doped ZnO NPs using *C. prostratus* flower extract *via* solution combustion synthesis offers a sustainable and efficient method for producing nanomaterials with tailored properties. The incorporation of Al^{3+} and Zr^{4+} ions into the ZnO lattice was successfully achieved without compromising the wurtzite crystal structure, as confirmed by PXRD and FTIR analyses. TEM, SEM-EDX characterizations revealed morphological changes and uniform dopant distribution, while UV-Vis spectroscopy indicated tunable band gap energies, with Zr-doped ZnO exhibiting the highest band gap of 3.77 eV. The crystallite sizes ranged from 8.8 nm (for 7 mol% Al-doped ZnO) to 16.1 nm (for 7 mol% Zr-doped ZnO). The application of these NPs in concrete blocks demonstrated that 7 mol% Zr-doped ZnO significantly enhances compressive strength to 49.96 MPa and provides antifungal properties, surpassing the performance of undoped and Al-doped counterparts. These findings underscore the potential of Zr-doped ZnO NPs as multifunctional additives in construction materials, offering both mechanical reinforcement and antimicrobial protection. Future research should focus on optimizing dopant concentrations and exploring the long-term durability and environmental impact of such nanocomposite materials in real-world applications.

Limitations and future plans

The current work gives us useful information about how to make Al- and Zr-doped ZnO nanoparticles in concrete and how well they can accomplish more than one thing. However, there are still certain limitations. There was no quantitative evaluation of antifungal action, including measuring inhibition zones and counting CFUs. This should be done in future work. Also, even though the antifungal action seemed to be surface-mediated, no surface coating was used, and the distribution of nanoparticles in the concrete matrix was not clearly defined. Future research will look at how to use surface-functionalized coatings, how long antifungal action lasts when exposed to the environment, and how to get the most nanoparticles into construction materials that can be scaled up.

Declarations:
Funding: *Nil;*
Conflict of interest*: None;*
Ethical approval*: Not applicable.*

REFERENCES

1. M.A. Beach, Nayanathara, U., Gao, Y., Zhang, C., Xiong, Y., Wang, Y. Such, G.K., *Chemical Reviews*, **124**(9), 5505 (2024).
2. A.N. Al-Thani, Jan, A.G., Abbas, M., Geetha, M. Sadasivuni, K.K. *Life Sciences*, 22899 (2024).
3. T. Yu, Chen, H., Hu, T., Feng, J., Xing, W., Tang, L. Tang, W., *Applied Catalysis B: Environmental*, **342,** 123401 (2024).
4. S. Kumar, Mirzaei, A., Kumar, A., Lee, M.H., Ghahremani, Z., Kim, T.U., Kim, J.Y., Kwoka, M., Kumar, M., Kim, S.S. Kim, H.W., *Coordination Chemistry Reviews*, **503**, 215657 (2024).
5. B. Rezaei, Yari, P., Sanders, S.M., Wang, H., Chugh, V.K., Liang, S., Mostufa, S., Xu, K., Wang, J.P., Gómez-Pastora, J. Wu, K., *Small*, **20**(5), 2304848 (2024).
6. M.Y. Al-darwesh, Ibrahim, S.S. Mohammed, M.A., *Results in Chemistry*, **7,** 101368 (2024).
7. J. Du, Arwa, A.H., Cao, Y., Yao, H., Sun, Y., Garaleh, M., Massoud, E.E.S., Ali, E., Assilzadeh, H. Escorcia-Gutierrez, J., *Environmental Research*, **258**, 119204 (2024).
8. S. Goswami, Bishnoi, A., Tank, D., Patel, P., Chahar, M., Khaturia, S., Modi, N., Khalid, M., Alam, M.W., Yadav, V.K. Alreshidi, M.A., *Inorganica Chimica Acta*, 122350 (2024).
9. G. Umadevi, K.G. Krishna, *Sensors and Actuators A: Physical*, **374**, 115479 (2024).

10. B. Ranjithkumar, D. Sudha, E.R. Kumar, S.S. Alharthi, *Ceramics International*, **50**(16), 27679 (2024).
11. B. Mahant, Patel, D., Kushwaha, O.S. Kumar, R., *Energy & Fuels*, **37**(24), 19621 (2023).
12. M. Vaseem, Umar, A. Hahn, Y.B., *Metal Oxide Nanostructures and Their Applications*, **5**(1), 10 (2010).
13. M. Abdi-Khanghah, Adelizadeh, M., Naserzadeh, Z. Barati, H. *Journal of Natural Gas Science and Engineering*, **54**, 120 (2018).
14. H. Jan, Shah, M., Andleeb, A., Faisal, S., Khattak, A., Rizwan, M., Drouet, S., Hano, C. Abbasi, B.H., *Oxidative Medicine and Cellular Longevity*, **2021**(1), p.4786227 (2021).
15. M. Ehsan, Waheed, A., Ullah, A., Kazmi, A., Ali, A., Raja, N.I., Mashwani, Z.U.R., Sultana, T., Mustafa, N., Ikram, M. Li, H., *BioMed Research International*, **2022**(1), 215183 (2022).
16. M. Alhujaily, Albukhaty, S., Yusuf, M., Mohammed, M.K., Sulaiman, G.M., Al-Karagoly, H., Alyamani, A.A., Albaqami, J. AlMalki, F.A. *Bioengineering*, **9**(10), 541 (2022).
17. G.K. Prashanth, Prashanth, P.A., Nagabhushana, B.M., Ananda, S., Krishnaiah, G.M., Nagendra, H.G., Sathyananda, H.M., Rajendra Singh, C., Yogisha, S., Anand, S. Tejabhiram, Y., *Artificial Cells, Nanomedicine, and Biotechnology*, **46**(5), 968 (2018).
18. G.K. Prashanth, Prashanth, P.A., Bora, U., Gadewar, M., Nagabhushana, B.M., Ananda, S., Krishnaiah, G.M. Sathyananda, H.M. *Karbala International Journal of Modern Science,* **1**(2), 67 (2015).
19. S. Nagarajaiah, Nanda, N., Manjappa, P., Nagabhushana, B.M., Gadewar, M., Rao, S. Krishna, P.G., *Applied Physics A*, **129**(6), 461 (2023).
20. P.G. Krishna, Ananthaswamy, P.P., Trivedi, P., Chaturvedi, V., Mutta, N.B., Sannaiah, A., Erra, A. Yadavalli, T., *Materials Science and Engineering*: C, **75**, 1026 (2017).
21. G. K, Prashanth, Prashanth P. A, Meghana Ramani, Ananda S, Nagabhushana B. M, Krishnaiah G. M, Nagendra H. G, Sathyananda H. M, Mutthuraju M, Rajendra Singh C. *BioNanoScience, e* **9** (4), 799 (2019).
22. Siddekha, Aisha, Lalithamba HS, and Prashanth GK. *Materials Research Innovations*, **29** (4), 215 (2025).
23. G.K. Prashanth, M. Gadewar, S. Rao, H.S. Lalithamba, S.H. Prashant, M. Mahadevaswamy, N.P. Bhagya, B.M. Nagabhushana, in: Advanced Materials in Engineering Applications, CRC Press, 2024, p. 329.
24. G.K. Prashanth, S. Rao, M. Gadewar, H.S. Lalithamba, M.M. Swamy, A.S. Sowmyashree, *Journal of Physics: Conference Series,* **2748 (**1), 012001, IOP Publishing, April, 2024.
25. G.K. Prashanth, A.S. Giresha, H.S. Lalithamba, M. Aman, S. Rao, K.N. Ravindra, M. Gadewar, N.P. Bhagya, M.M. Swamy, V. Chaturvedi, *Inorganic Chemistry Communications*, **171**, 113592 (2025).
26. V.U. Nallal, Prabha, K., Muthupandi, S. Razia, M., *Materials Today: Proceedings*, **49**, 2632 (2022).
27. N.T.T. Nguyen, Nguyen, L.M., Nguyen, T.T.T., Nguyen, D.T.C. Tran, T.V., *Environmental Chemistry Letters*, **20**(4), 2531 (2022).
28. S. Ahmed, Chaudhry, S.A. Ikram, S., *Journal of Photochemistry and Photobiology B: Biology*, **166**, 272 (2017).
29. V. Mohammadzadeh, Barani, M., Amiri, M.S., Yazdi, M.E.T., Hassanisaadi, M., Rahdar, A. Varma, R.S., *Sustainable Chemistry and Pharmacy*, **25**, 100606 (2022).
30. A. Balkrishna, Thakur, P. Varshney, A., *Frontiers in Pharmacology*, **11**, 171 (2020).
31. E. Ghafari, Ghahari, S.A., Feng, Y., Severgnini, F. Lu, N., *Composites Part B: Engineering*, **105**, 160 (2016).
32. F.E.Z.M. Mostafa, Smarzewski, P., El Hafez, G.M.A., Farghali, A.A., Morsi, W.M., Faried, A.S. Tawfik, T.A., *Materials*, **16**(21), 6909 (2023).
33. B.O. Bica, J.V.S. de Melo, *Construction and Building Materials*, **252**, 119120 (2020).
34. M. Kumar, M. Bansal, R. Garg, *Materials Today: Proceedings*, **43**, 892 (2021).
35. M.G. Faraj, Ibrahim, K. Salhin, A., *Materials in Semiconductor Processing*, **15**(2), 206 (2012).
36. R.B.M. Cross, De Souza, M.M. Narayanan, E.S., *Nanotechnology*, **16**(10), 2188 (2005).
37. S.H. Moon, Choi, J.H., Chae, K.W., Kim, J.S. Cheon, C.I., *Ceramics International*, **39**(3), 2431 (2013).
38. S. Baruah, Dutta, J., *Science and Tec*h*nology of Advanced Materials*, **10**(1), 013001 (2009).
39. X. Yang, Takeichi, N., Shida, K., Tanaka, H., Kuriyama, N. Sakai, T., *Journal of Alloys and Compounds*, **509**(4), 1211 (2011).
40. M. Golmohammadi, Towfighi, J., Hosseinpour, M. Ahmadi, S.J., *The Journal of Supercritical Fluids*, **107**, 699 (2016).
41. H. Ueda, Tanaka, Y., Wakabayashi, Y. Kimura, T., *Physica B: Condensed Matter*, **536**, 118 (2018).
42. X. Zha, Yang, C., Huang, X., Ding, J. Ding, Z., *Environmental Pollutants and Bioavailability*, **36**(1), 2376827 (2024).
43. S. Özkar, *Applied Surface Science,* 2, **56 (**5), 1272 (2009).
44. I. Khan, Khan, S., Nongjai, R., Ahmed, H. Khan, W., *Optical Materials*, **35**(6), 1189 (2013).
45. K. A. Nxumalo, J. O. Adeyemi, T. B. Leta, T. M. Pfukwa, S. N. Okafor, O. A. Fawole, *Scientific Reports* **14**(1), 18071 (2024).
46. S. Bhattacharyya, Sh. Akhtar, A. Chaudhuri, Sh. Mahanty, P. Chaudhuri, M. Sudarshan, *Case Studies in Construction Materials,* **17,** e01258 (2022).
47. Y. N. Slavin, H. Bach, *Nanomaterials,* **12** (24), 4470 (2022), https://doi.org/10.3390/nano12244470.